

Making spin-orbit coupling visible in single layer ferrimagnets: direct observation of spin-orbit torques and chiral spin textures

Sachin Krishnia^{1,*†}, Eloi Haltz^{1,*}, Léo Berges¹, Lucia Aballe², Michael Foerster², Laura Bocher¹, Raphaël Weil¹, André Thiaville¹, João Sampaio¹, and Alexandra Mougin¹

¹Université Paris-Saclay, CNRS, Laboratoire de Physique des Solides, 91405, Orsay, France.

²Alba Synchrotron Light Facility, CELLS, Barcelona, E-08290, Spain.

Abstract

We demonstrate that effects of spin-orbit coupling (SOC) and inversion asymmetry: spin-orbit torques (SOTs), Dzyaloshinskii-Moriya interaction (DMI) and chiral magnetism can co-exist in a single layer ferrimagnetic GdFeCo without any heavy metal interface. We unambiguously measure net damping-like and field-like SOTs. We quantify the DMI ($D = -8 \mu\text{J/m}^2$) and we observe the resulting chiral magnetic textures. In a similar film capped with Pt, we retrieve the well-known interfacial effects. These additional internal SOC effects open a new path to design efficient spintronic materials.

Magnetic layers interfaced with materials with strong spin-orbit coupling (SOC) (such as Pt, Ta) manifest several fascinating phenomena when the inversion symmetry is broken^{1–4}. One direct consequence of SOC is the interplay between charge and spin transport *via* spin Hall effect (SHE) in heavy metals, which leads to non-equilibrium spin accumulation at the surfaces^{5,6}. Another mechanism, the Rashba effect, arises when the electrical carriers move in an interfacial electric field and experience the resultant magnetic field that couples with their spins^{7,8}. Both mechanisms give rise to spin-orbit torques (SOTs) in the magnetic layer, with damping-like and field-like components^{9–11}. Surprisingly, recently, SOTs have been detected in a single layer NiFe even in the absence of heavy metal adjacent layers films^{12,13}. The SOTs are an efficient way to manipulate chiral magnetic textures, such as Néel domain walls (DWs)^{2,3} and skyrmions¹⁴, whose chirality is induced by another product of SOC, the Dzyaloshinskii-Moriya interaction (DMI)¹.

Recently, the combination of SOTs and DMI has enabled fast and efficient magnetization dynamics in rare earth (RE)-transition metal (TM) ferrimagnetic films interfaced with a heavy metal^{15,16}. In conventional 3d-TM/heavy metal bilayers, Pt 5d (or Pd 4d) states hybridize strongly

[†] sachin.krishnia@u-psud.fr

with the 3d states of the TM leading to proximity effects and an enhanced orbital moment^{8,17}. In RE-TM alloys, spintronic effects are described by the combination of localized 4f magnetism and itinerant magnetism of the *spd* band structure¹⁸. It was shown earlier that the itinerant magnetism is dominated by RE 5d and TM 3d states¹⁷. This hybridization implies that RE atoms with unpaired 5d electrons may exhibit large SOC^{19–21}, suggesting that SOT and DMI could appear even in the absence of an adjacent heavy metal layer. Very recent observation of interfacial DMI in Tm and Tb based oxide garnets is attributed to the orbital moment of the RE^{22,23}. Furthermore, an interface-independent DMI originated in the bulk of a GdFeCo ferrimagnet layer has been reported using indirect methods based on asymmetric magnetic reversal²⁴, which was attributed to a broken symmetry caused by inhomogeneity of RE atoms along the film thickness. On the other hand, experiments on $[Co/Tb]_n$ multilayers did not show any SOT contribution from the RE²⁵. The underlying origin of SOC and the role of RE (especially Gd which has no orbital momentum) on SOC in ferrimagnets hence remain to be understood and need to be addressed by experimental evidence.

In this letter, we aim to provide direct evidence of the internal SOC effects in single layer GdFeCo ferrimagnets. The SOC induced effects such as SOTs, DMI and chiral magnetic textures, are observed in a GdFeCo without any heavy metal layer, but with a symmetry-breaking inhomogeneous Gd concentration along the thickness, a key ingredient to observe the SOC effects.

$Gd_{0.35}(Fe_{85}Co_{15})_{0.65}$ ferrimagnetic thin films of 5 nm thickness were deposited on thermally-oxidised Si substrates by e-beam co-evaporation of Gd and FeCo targets in ultra-high vacuum chamber ($\sim 10^{-10}$ mbar)²⁶. Al (5 nm) and Pt (7 nm) capping layers were deposited to prevent oxidation of the ferrimagnets. The Pt capped sample is used as a reference sample and, hereafter, the GdFeCo refers to Al-capped sample unless mentioned. The GdFeCo thin film is composed of two sub-lattices of Gd (RE) and FeCo (TM) coupled antiferromagnetically²⁷. Magnetization as a function of temperature is shown in Figure 1(a). At the magnetic compensation temperature, $T_M \approx 275K$ for this sample, the net magnetization vanishes and the coercive field diverges (Figure 1b).

To measure the Hall effect, the films were patterned into 5 μm wide Hall cross structures using e-beam lithography and a hard-mask etching technique. Figure 1(c) and (d) show hysteresis loops obtained by anomalous Hall effect below and above T_M . The electrical properties are dominated by the TM sub-lattice and, therefore, the change of sign of the Hall resistance (R_{AHE}) across T_M is a signature of the reversal of the alignment of FeCo with the external field, as shown

in the insets. The effective anisotropy field (H_k ; Figure 1(b) in blue), obtained by fitting R_{AHE} versus in-plane field²⁸, diverges at T_M .

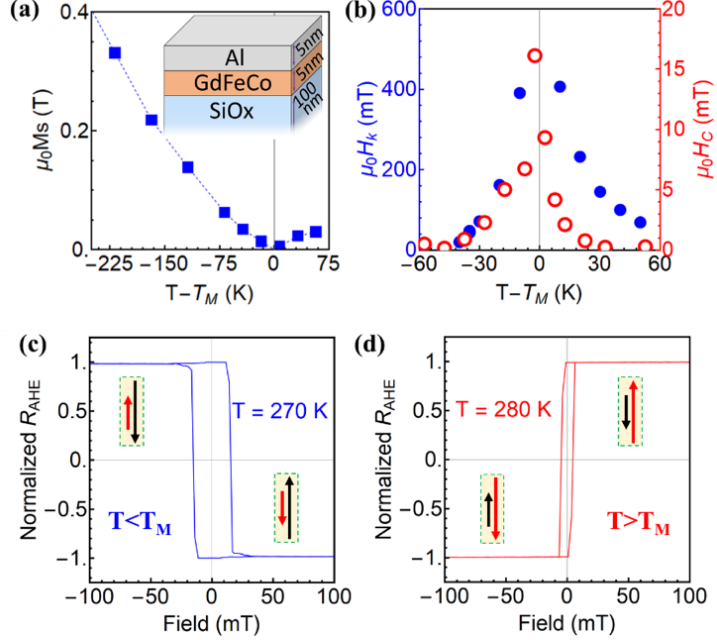


Figure 1. (a) Net magnetization (M_s) versus temperature measured using superconducting quantum interference device (SQUID) magnetometer. (b) Anisotropy field (H_k) in blue and coercive field (H_c) in red as a function of temperature, which diverge at T_M . (c,d) Normalised R_{AHE} vs perpendicular magnetic field at (c) $T = 270$ K $< T_M$ and (d) $T = 280$ K $> T_M$. The arrows represent the direction and relative magnitude of Gd (black) and FeCo (red) magnetic moments.

To investigate the existence of SOC inside the ferrimagnetic layer, first we quantify the two components of current-induced torques by using second harmonic Hall voltage measurement technique⁹. The measurement geometries are shown in Figure 2(a,b). This technique uses an ac current of low frequency ($f = 1.33$ kHz) to induce periodic magnetization oscillations, which modulate the R_{AHE} at frequency f and the anomalous Hall voltage at frequency $2f$. By measuring simultaneously the first and second harmonics as a function of the in-plane field (H) applied along or transverse to the current direction (H/I_{AC} and $H \perp I_{AC}$, Figure 2a,b), we extract the damping-like (H_{DL}) or field-like (H_{FL}) effective fields (see suppl. mat.). To be able to measure small effects, the analysis of second harmonic method was improved to account the magnetic fields larger than anisotropy fields.

Figure 2(c) shows the temperature dependence of H_{DL} per current density (H_{DL}/J) in GdFeCo layer. At a given temperature, H_{DL} changes sign when the magnetization is reversed, in agreement with the expected symmetry of SHE induced torque: $\vec{H}_{DL} = H_{DL}(\hat{m} \times \hat{\sigma})$, where \hat{m} and $\hat{\sigma}$ are the unit vectors along magnetization and spin polarization directions²⁹. Assuming that SHE

is the main source of H_{DL} , we expect that $\mu_0 H_{DL} = \frac{\hbar}{2e} \frac{1}{M_s t} J \theta_{SH}$, where θ_{SH} is the spin Hall angle and should be temperature independent for a given material. H_{DL}/J diverges at $T \rightarrow T_M$, showing the expected scaling with $1/M_s$. We find $\theta_{SH} \approx 7 \times 10^{-4} > 0$ (figure 2e), which is ~ 100 x smaller than the Co/Pt interfacial effect ($\theta_{SH} \sim 5 \times 10^{-2}$ in Co/Pt)³⁰. θ_{SH} is independent of temperature, in particular not changing across T_M , which is consistent with hypothesis of SHE as the main source of H_{DL} .

Figure 2(d) shows the H_{FL} per current density (H_{FL}/J) at various temperatures below the compensation temperature. We could not extract reliably the H_{FL} above the compensation temperature due to increasing noise with temperature (see suppl.). At a fixed temperature, H_{FL} does not change sign with the reversal of the magnetization, as expected with the symmetry: $\vec{H}_{FL} = H_{FL} \hat{\sigma}$. In addition to SOTs, the current generates an Oersted field (H_{Oe}) that is independent of M_s but has the same orientation as H_{FL} . Therefore, H_{Oe} contributes to the measured H_{FL} (see line in Fig. 2d). However, the divergence of H_{FL} as $T \rightarrow T_M$ shows that a non-Oersted torque is present. Assuming a Rashba-induced H_{FL} , it would depend on M_s with a relation $\mu_0 H_{FL} = -\frac{2 m_e}{\hbar e M_s} \alpha_R P J$, where m_e is the mass of the electron, P is the current polarization and α_R is the Rashba parameter. This relation matches well with the obtained variation of H_{FL} . Figure 2(f) shows the extracted $\alpha_R P$ at various temperatures. The obtained value of $\alpha_R P \approx 7 \times 10^{-33} J m$ is independent of the temperature, suggesting the presence of significant SOT-induced H_{FL} . The existence of these SOTs in a ferrimagnetic layer without an adjacent heavy metal suggests the presence of an internal SOC from the magnetic layer itself.

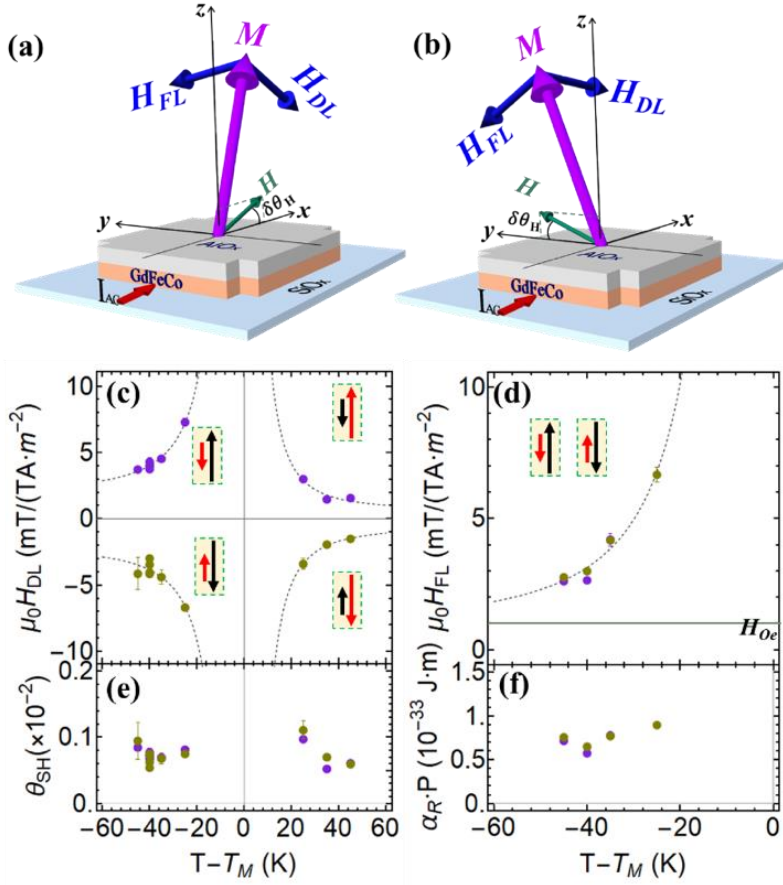


Figure 2 (a,b) Illustration of harmonic Hall measurement in **(a)** longitudinal and **(b)** transverse geometries to obtain the H_{DL} and H_{FL} . H and I_{ac} are the applied magnetic field and ac current. **(c)** H_{DL} and **(d)** H_{FL} per current density as a function of temperature. Purple (khaki) points correspond to an up (down) saturated state. The diagrams represent the direction and magnitude of Gd (black) and FeCo (red) magnetic moments. The dotted lines are guides to the eyes. The estimated Oersted field ($\sim 1 \text{ mT/TA}\cdot\text{m}^{-2}$) due to I_{ac} is shown by a line. **(e)** Spin Hall angle (θ_{SH}) and **(f)** Rashba parameter ($\alpha_R P$) vs temperature.

Another phenomenon induced by SOC is the DMI, which favours chiral magnetic textures^{15,31,32}. We examine the internal structure of DWs in the ferrimagnetic film using photoemission electron microscopy combined with X-ray magnetic circular dichroism (XMCD-PEEM)³³. In our experiment, the incident X-ray energy was set to the Gd $M_{4,5}$ absorption edge at a grazing angle of 16° (see Fig. 3a). In XMCD, the contrast is proportional to $\hat{k}_{X-ray} \cdot \hat{m}$ (where \hat{k}_{X-ray} is the unit vector along the incident beam), resulting in 3.5x higher in-plane than that of out-of-plane contrast. Therefore, Néel and Bloch DWs, as well as their chirality, can be distinguished by their different XMCD-PEEM profiles³², even when the DW width (Δ) is smaller than the microscope resolution (r) (see Fig. 3b).

The imaging was performed at $T = 230 \text{ K} < T_M$, in order to avoid thermal magnetization fluctuations. Figure 3(c) shows typical XMCD-PEEM images of up and down domains manifested

by light and dark grey contrasts, respectively (more images in suppl. mat.). Interestingly, an intense black or white contrast appears between the domains when the DW length is perpendicular to the incident beam, while it is absent when the incident beam is along the DW length. The intense DW contrast is clearly visible on the XMCD line-scans (Figure 3d), as evidenced by either a peak or a dip between the dark and light grey domains. This pattern shows that the DW magnetization lies parallel or antiparallel to the X-ray beam, that is, the DW is chiral Néel DW with a left-handed chirality. To acquire the DWs width and internal magnetization direction, we fit the obtained XMCD line scans with the expected profile convoluted with a Gaussian function to account for the microscope resolution. By fitting several line-scans of DWs with different orientations with the theoretical XMCD profile keeping the azimuthal angle (φ) and Δ as free parameters (figure 3d), we obtained $\varphi = 180 \pm 10^\circ$ (left-handed Néel) and $\Delta = 20 \pm 10$ nm ($r = 60$ nm was measured on dust particles in the image). As the ferrimagnetic film is not interfaced with any heavy metal, these chiral Néel DWs clearly indicate the existence of DMI in the volume of the film.

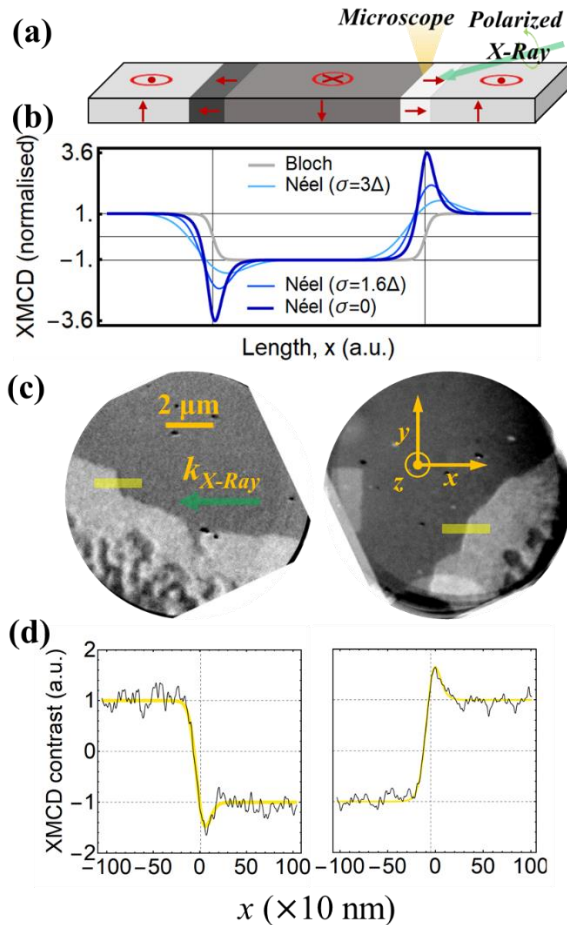


Figure 3 (a) Schematic of the XMCD-PEEM experiment, showing the magnetization profile of an up-down and down-up left-handed Néel DWs and the X-ray beam with grazing incidence (16°) and perpendicular to the DW length. (b) Calculated normalised XMCD-PEEM intensity profile for DWs in (a), taking into account the finite microscope resolution (r ; blue curves). The gray curve is the profile of Bloch DWs. (c)

Multidomain XMCD-PEEM images at the Gd M_{4,5} edge (1178.7 eV). The green arrow shows the direction of the X-ray beam. The dark (bright) contrast corresponds to a down (up) magnetic domain. The analysed DWs are in the vicinity of a region of lowered anisotropy induced by long exposure to the X-rays (with small domains; in the bottom). (d) Intensity profiles (black lines) averaged over the yellow regions in (c). The thick yellow line is a fit to the experimental data using the theoretical profile as shown in (a) with $r = 60$ nm that was measured on dust particles in the image.

In order to quantify the magnitude and sign of this DMI, we perform spin-wave (SW) spectroscopy experiments using Brillouin light scattering (BLS) technique in Damon-Eshbach geometry (see inset in Figure 4a) at room temperature (293 K)³⁴. This method measures two resonance frequencies corresponding to the Stokes and anti-Stokes modes (f_S and f_{AS}) (Fig. 4a), which correspond to counter-propagating SWs. Due to DMI, they have different frequencies. The variation of this difference $\Delta f = f_{AS} - f_S$ with the incident wave vector k_{sw} is directly proportional to the DMI parameter D : $\Delta f = -\frac{2\gamma}{\pi M_s} D k_{sw}$, with γ being the gyromagnetic ratio of the alloy (see Suppl.)^{34,35}.

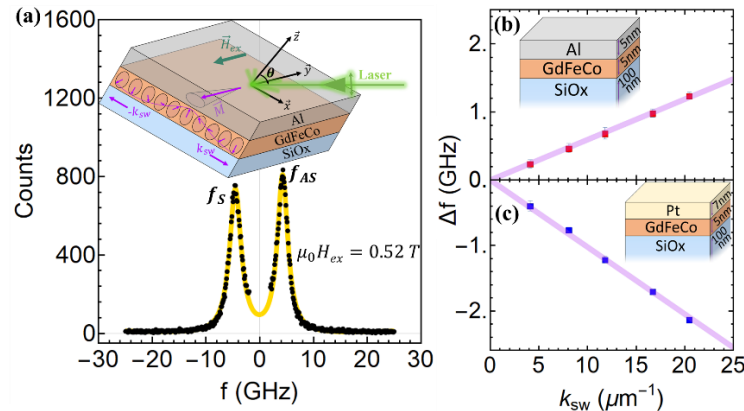


Figure 4 (a) BLS spectra of SiOx/GdFeCo/Al obtained using a laser beam of wavelength of 532 nm at 293 K under an in-plane magnetic field $\mu_0 H_{ex} = 0.52$ T and at beam incidence angle (θ) = 60° (corresponding to $|k_{sw}| = 20.46 \mu\text{m}^{-1}$). The yellow lines are Lorentzian fits to the experimental data (black circles). The inset shows measurement geometry. (b,c) The DMI-induced frequency shifts (Δf) of nonreciprocal spin waves *vs* wave vector magnitudes $|k_{sw}|$ for (b) Al-covered (Red) and (c) Pt-covered (Blue) film. The thick lines are the linear fit.

A typical BLS spectrum for the same sample is shown in figure 4(a) and the dependency of Δf with k_{sw} is shown in Figure 4(b). A value of $D = -8.4 \pm 2.5 \mu\text{J/m}^2$ is obtained from Δf *vs* k_{sw} . This DMI magnitude is much smaller than Ta/Co and Pt/Co systems³⁵.

To understand the stabilization of Néel DWs in low-DMI systems, we must consider the critical DMI ($D_C = \frac{4}{\pi} \Delta K \approx \frac{2 \ln 2}{\pi^2} t \mu_0 M_S^2$) required to form a Néel DW in thin films¹. Due to the low M_S of this system, D is indeed ~ 4 x larger than the estimated D_C at the temperature of the PEEM experiments ($D_C \approx 2.3 \mu\text{J/m}^2$). These calculations show that the extracted D agrees with

left-handed chirality ($D < 0$) and favours Néel DWs structure ($|D| > D_C$) as observed in PEEM experiments, and how a small DMI energy inside the ferrimagnet can dominate over the demagnetizing energy.

Further insights into the interfacial SOC contributions are obtained by comparing the θ_{SH} and D of Si/SiO_x(100nm)/GdFeCo(5nm)/Pt(7nm) sample. We find a median value of $\theta_{SH} = -0.12$ in GdFeCo/Pt sample (see suppl.). Similarly, to the Al capped ferrimagnetic sample, the θ_{SH} is found to be independent of temperature, however the sign is opposite. The D for the Pt capped sample was determined: $D = (27.2 \pm 0.2) \mu\text{J}/\text{m}^2$ (figure 4c). The magnitude and sign agree with the naïve expectation considering the Co concentration (~10%) and the known value for Co/Pt³⁵. The sign of the DMI in SiO_x/GdFeCo/Pt sample is found to be opposite to that of SiO_x/GdFeCo/Al sample. Assuming that the films are the same, the interfacial DMI and SOTs produced at the Pt interface dominate over the internal effects, unlike what was found for DMI in another study²⁴.

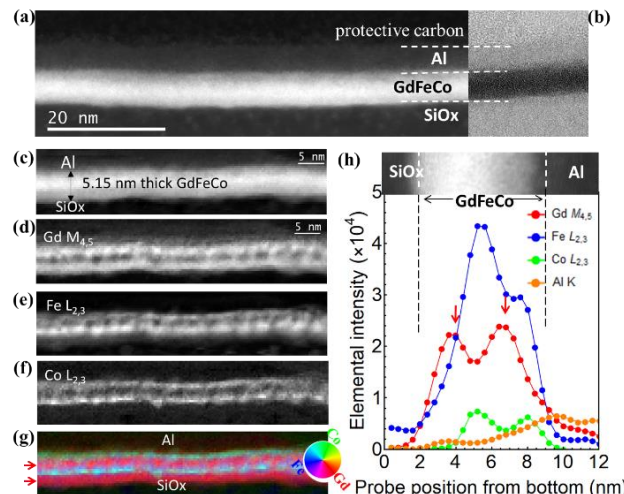


Figure 5 (a) HAADF and (b) BF STEM images of the SiO_x/GdFeCo/Al cross-section. (c) HAADF intensity map of the probed area with the corresponding elemental maps extracted at the (d) Gd M_{4,5}, (e) Fe L_{2,3}, (f) Co L_{2,3} edges. (g) Superimposed “false color” map of Gd (red), Fe (blue), and Co (green). (h) Laterally integrated line profiles over a length of 12 nm of the Gd M_{4,5} (red), Co L_{2,3} (green), Fe L_{2,3} (blue) and Al K (orange) intensities along the film thickness.

The presence of DMI and SOT in thin films without a heavy metal adjacent layer is far from trivial, and suggests that its origin issues from the intrinsic properties of the magnetic film. The occurrence of these phenomena requires a broken inversion symmetry and a strong spin-orbit coupling. The SOC may arise from the RE atoms, as discussed previously. To investigate the origin of the broken inversion symmetry in the film, electron energy-loss spectroscopy (EELS) studies were performed in a scanning transmission electron microscopy (STEM) in cross-sectional views

of the film^{23,24,26}. Typical high-angle annular dark-field (HAADF) and bright-field (BF) STEM images of the SiO_x/GdFeCo/Al film are shown in figures 5(a) and (b), respectively. The GdFeCo layer can be clearly identified by the higher contrast in the HAADF image, while both SiO_x and AlO_x layers are distinguishable by their lower contrasts. The ferrimagnet layer presents a homogeneous thickness of ca. 5.2 ± 0.4 nm, with defined bottom and top interfaces running along the observed film (see suppl. fig. S16). The BF image presents a clear amorphous contrast in the GdFeCo alloy across the full thin film thickness, which rules out any non-centrosymmetric crystal structure.

Next, we reveal by EELS a non-uniform elemental distribution in the GdFeCo amorphous layer, in agreement with our previous observations in other rare earth/transition metal films²⁶. The elemental maps and profiles (Figures 5c to e) clearly evidence an anti-correlated spatial distribution of the Gd (Fig. 5d) and the 3d TM elements (Fe in Fig. 5e and Co in Fig. 5f), throughout the ferrimagnetic layer (see suppl., fig. S17). This peculiar elemental dissociation is present along the whole amorphous film, while its depth-distribution is nanostructured as follows: a first Gd-rich layer of ca. 1.6 nm at the bottom interface, followed by a first FeCo-rich intermediate layer of ca. 1.2 nm, then a second Gd-rich layer of ca. 1.2 nm, and finally a thin FeCo-rich layer of ca. 1 nm at the top interface. Furthermore, while the Gd-rich layers appear homogeneous along the entire film (marked by red arrows in Figs. 5 g and h), the FeCo-rich layers form aggregated nanostructures separated regularly by 2.8 ± 0.4 nm. These findings highlight a nanostructure alternating between Gd- and FeCo-rich sub-layers, in contrast with previous work reported for thicker GdFeCo films²⁴. This elemental inhomogeneity breaks the spatial inversion symmetry and enables the emergence of net SOC effects inside the GdFeCo layer.

In summary, we have measured a net SOT, a significant DMI, and chiral Néel DWs in a single thin ferrimagnetic layer without any heavy-metal interface. This is a threefold experimental evidence of internal SOC and breaking of inversion symmetry. We attribute the SOC to the electronic hybridization of RE-5d and TM-3d electrons, which enables spin-orbit effects to occur even for Gd, with half-filled 4f electron shell^{18,20,21}. The source of the symmetry breaking is the elemental inhomogeneity along the depth direction. The internal DMI and SOTs superimpose with the interfacial effects and, therefore, should not be overlooked in the analysis of stability and dynamics of magnetic textures where the DMI and SOTs are the core elements. Moreover, these internal effects could be engineered by tuning the composition profile along the film thickness. Our findings not only provide new insights into the physics of ferrimagnetic alloys but also open new paths to design and engineer novel materials for ultrafast spintronics applications.

Data availability

The data are available from the corresponding author upon reasonable request.

Acknowledgements

We are very thankful to Stanislas Rohart for fruitful discussions, Richard Mattana for the SQUID measurements of M_S , and Nathalie Brun for assistance with the analysis of the STEM data. S. K., and E. H. acknowledge public grant overseen by the ANR as part of the “Investissements d’Avenir” programme (Labex NanoSaclay, reference: ANR-10-LABX-0035) for the FEMINIST project and travelling grants. S. Krishnia acknowledges a public grant from PIAF ANR-17-CE09-0030. The transport measurements were supported by Université Paris-Sud Grant MRM PMP. We acknowledge funding from the ANR under the “Investissements d’Avenir” programme TEMPOS (reference: ANR-10_EQPX-50) for the FIB access.

S.K. and E.H. contributed equally. The experiments were conceived and designed by S.K., E.H., J.S., and A.M. Samples were prepared by E.H., and R.W. Transport measurements were made by S.K., L. Berge, and J.S. XPEEM experiments were performed by M.F., L.A., E.H., J.S., S.K., and A.M. BLS measurements were performed by S.K., and A.T. STEM experiments and analysis were done by L. Bocher. Data analysis and calculations were made by S.K., E.H., L. Berge, J.S., and A.M. All authors prepared and discussed the manuscript.

Additional information

Supplementary information is available.

References

1. Thiaville, A., Rohart, S., Jué, É., Cros, V. & Fert, A. Dynamics of Dzyaloshinskii domain walls in ultrathin magnetic films. *Epl* **100**, (2012).
2. Emori, S., Bauer, U., Ahn, S.-M., Martinez, E. & Beach, G. S. D. Current-driven dynamics of chiral ferromagnetic domain walls. *Nat. Mater.* **12**, 611–616 (2013).
3. Ryu, K.-S., Thomas, L., Yang, S.-H. & Parkin, S. Chiral spin torque at magnetic domain walls. *Nat. Nanotechnol.* **8**, 527–533 (2013).
4. Soumyanarayanan, A., Reyren, N., Fert, A. & Panagopoulos, C. Emergent phenomena induced by spin-orbit coupling at surfaces and interfaces. *Nature* **539**, 509–517 (2016).
5. Dyakonov, M. I. & Perel, V. I. Current-induced spin orientation of electrons in semiconductors. *Phys. Lett. A* **35**, 459–460 (1971).
6. Stamm, C. *et al.* Magneto-Optical Detection of the Spin Hall Effect in Pt and W Thin Films. *Phys. Rev. Lett.* (2017) doi:10.1103/PhysRevLett.119.087203.
7. Sánchez, J. C. R. *et al.* Spin-to-charge conversion using Rashba coupling at the interface between non-magnetic materials. *Nat. Commun.* **4**, 1–7 (2013).
8. Manchon, A. & Belabbes, A. *Spin-Orbitronics at Transition Metal Interfaces. Solid State Physics - Advances in Research and Applications* vol. 68 (Elsevier Inc., 2017).
9. Kim, J. *et al.* Layer thickness dependence of the current-induced effective field vector in Ta|CoFeB|MgO. *Nat. Mater.* **12**, 240–245 (2013).
10. Liu, L. *et al.* Spin-torque switching with the giant spin hall effect of tantalum. *Science (80-.).* **336**, 555–558 (2012).
11. Garello, K. *et al.* Symmetry and magnitude of spin-orbit torques in ferromagnetic heterostructures. *Nat. Nanotechnol.* **8**, 587–593 (2013).
12. Emori, S. *et al.* Interfacial spin-orbit torque without bulk spin-orbit coupling. *Phys. Rev. B* **93**, 1–5 (2016).
13. Wang, W. *et al.* Anomalous spin-orbit torques in magnetic single-layer films. *Nat. Nanotechnol.* **14**, 819–824 (2019).
14. Sampaio, J., Cros, V., Rohart, S., Thiaville, A. & Fert, A. Nucleation, stability and current-induced motion of isolated magnetic skyrmions in nanostructures. *Nat. Nanotechnol.* **8**, 839–844 (2013).
15. Caretta, L. *et al.* Fast current-driven domain walls and small skyrmions in a compensated ferrimagnet. *Nat. Nanotechnol.* **13**, 1154–1160 (2018).
16. Haltz, E. *et al.* Precession-free domain wall dynamics in compensated ferrimagnets. <http://arxiv.org/abs/1908.08867> (2019).
17. Brooks, M. S. S., Nordstrom, L. & Johansson, B. 3d-5d band magnetism in rare earth-transition metal intermetallics: Total and partial magnetic moments of the RFe₂ (R=Gd-Yb) Laves phase compounds. *J. Phys. Condens. Matter* **3**, 2357–2371 (1991).
18. Coffey, D. *et al.* Antiferromagnetic Spin Coupling between Rare Earth Adatoms and Iron Islands Probed by Spin-Polarized Tunneling. *Sci. Rep.* **5**, 1–7 (2015).
19. Laguna-Marco, M. A., Chaboy, J. & Piquer, C. Experimental determination of the R(5d)-T(3d) hybridization in rare-earth intermetallics. *Phys. Rev. B* **77**, 125132 (2008).
20. Jang, H. *et al.* Observation of orbital order in the half-filled 4f Gd compound. *Phys. Rev. Lett.* **117**, 1–5 (2016).

21. Schulz, S. *et al.* Emerging 2D-ferromagnetism and strong spin-orbit coupling at the surface of valence-fluctuating EuIr₂Si₂. *npj Quantum Mater.* **4**, (2019).
22. Vélez, S. *et al.* High-speed domain wall racetracks in a magnetic insulator. *Nat. Commun.* **10**, 1–8 (2019).
23. Caretta, L. *et al.* Interfacial Dzyaloshinskii-Moriya interaction arising from rare-earth orbital magnetism in insulating magnetic oxides. *Nat. Commun.* **11**, 1–9 (2020).
24. Kim, D. H. *et al.* Bulk Dzyaloshinskii–Moriya interaction in amorphous ferrimagnetic alloys. *Nat. Mater.* **18**, 685–690 (2019).
25. Yu, J. *et al.* Long spin coherence length and bulk-like spin–orbit torque in ferrimagnetic multilayers. *Nat. Mater.* **18**, 29–34 (2019).
26. Haltz, E. *et al.* Deviations from bulk behavior in TbFe(Co) thin films: Interfaces contribution in the biased composition. *Phys. Rev. Mater.* **2**, 1–9 (2018).
27. Hansen, P., Clausen, C., Much, G., Rosenkranz, M. & Witter, K. Magnetic and magneto-optical properties of rare-earth transition-metal alloys containing Gd, Tb, Fe, Co. *J. Appl. Phys.* **66**, 756–767 (1989).
28. Wood, R. Exact solution for a Stoner-Wohlfarth particle in an applied field and a new approximation for the energy barrier. *IEEE Trans. Magn.* **45**, 100–103 (2009).
29. Khvalkovskiy, A. V. *et al.* Matching domain-wall configuration and spin-orbit torques for efficient domain-wall motion. *Phys. Rev. B - Condens. Matter Mater. Phys.* **87**, 020402 (2013).
30. Rojas-Sánchez, J. C. *et al.* Spin pumping and inverse spin hall effect in platinum: The essential role of spin-memory loss at metallic interfaces. *Phys. Rev. Lett.* **112**, 106602 (2014).
31. Streubel, R. *et al.* Experimental Evidence of Chiral Ferrimagnetism in Amorphous GdCo Films. *Adv. Mater.* **30**, 1–8 (2018).
32. Boulle, O. *et al.* Room-temperature chiral magnetic skyrmions in ultrathin magnetic nanostructures. *Nat. Nanotechnol.* **11**, 449–454 (2016).
33. Aballe, L., Foerster, M., Pellegrin, E., Nicolas, J. & Ferrer, S. The ALBA spectroscopic LEEM-PEEM experimental station: Layout and performance. *J. Synchrotron Radiat.* **22**, 745–752 (2015).
34. Di, K. *et al.* Direct observation of the Dzyaloshinskii-Moriya interaction in a Pt/Co/Ni film. *Phys. Rev. Lett.* **114**, 1–5 (2015).
35. Belmeguenai, M. *et al.* Interfacial Dzyaloshinskii-Moriya interaction in perpendicularly magnetized Pt/Co/AlO_x ultrathin films measured by Brillouin light spectroscopy. *Phys. Rev. B - Condens. Matter Mater. Phys.* **91**, 1–4 (2015).

Supplementary information

Making spin-orbit coupling visible in single layer ferrimagnet: direct observation of spin-orbit torques and chiral spin textures

Sachin Krishnia^{1,*†}, Eloi Haltz^{1,*}, Léo Berges¹, Lucia Aballe², Michael Foerster², Laura Bocher¹, Raphaël Weil¹, André Thiaville¹, João Sampaio¹, and Alexandra Mougin¹

¹Université Paris-Saclay, CNRS, Laboratoire de Physique des Solides, 91405, Orsay, France.

²Alba Synchrotron Light Facility, CELLS, Barcelona, E-08290, Spain.

Table of contents:

- S1 Modulation of magnetization due to current-induced effective fields and harmonic Hall voltage expression**
- S2 Spin-orbit torques analysis in SiOx/GdFeCo/Al sample**
- S3 Spin-orbit torques analysis in SiOx/GdFeCo/Pt sample**
- S4 XMCD-PEEM imaging on SiOx/GdFeCo/Al**
- S5 Spin wave spectroscopy to quantify DMI in SiOx/GdFeCo/Al sample**
- S6 STEM and EELS studies on SiOx/GdFeCo/Al sample**
- S7 References**

[†] Corresponding author: sachin.krishnia@u-psud.fr

S1 Modulation of magnetization due to current-induced effective fields and harmonic Hall voltage expression

The SiO_x/GdFeCo/Al sample exhibits tiny internal SOC effects. To obtain accurate and precise SOT fields, we modify the analysis of the harmonic Hall voltage method to accommodate the behavior of V_{2f} with magnetic fields applied in a range between zero to $H \gg H_k$. This new approach allows us to deduce the SOT fields with increased accuracy compared with the results obtained with the conventional approach, which uses $H \ll H_k$ ¹.

When an ac current is injected into a heavy metal/magnetic material bi-layer, it induces effective magnetic fields (ΔH) on the magnetization due to various phenomena: Oersted field, or torques due to generated spin currents. The ΔH induces oscillations of the magnetization around its equilibrium position (θ, ϕ) in synchronization with ac frequency (f) (Fig. S1). The magnitude of these oscillations ($\Delta\theta, \Delta\phi$) not only depends on the effective field induced by the current, but also on the external field H , the anisotropy of the sample H_k , etc. By measuring the variation of ($\Delta\theta, \Delta\phi$) as a function of applied fields, it is possible to extract the components of the current-induced effective field ΔH .

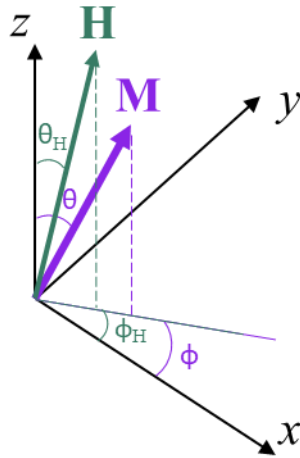


Figure S1. A schematic showing the directions of magnetization and external magnetic field in cartesian coordinates system.

Using the Taylor's expansion, $\Delta\theta$, and $\Delta\phi$ can be expressed as:

$$\Delta\theta = \frac{\partial_{H_x} E}{\partial_\theta E} \Delta H_x + \frac{\partial_{H_y} E}{\partial_\theta E} \Delta H_y + \frac{\partial_{H_z} E}{\partial_\theta E} \Delta H_z \quad \& \quad \Delta\phi = \frac{\partial_{H_x} E}{\partial_\phi E} \Delta H_x + \frac{\partial_{H_y} E}{\partial_\phi E} \Delta H_y + \frac{\partial_{H_z} E}{\partial_\phi E} \Delta H_z, \quad (1)$$

with E is the total energy density of the thin film. For a film with uniaxial anisotropy, the energy density can be expressed as:

$$E = -K_{eff} \cos^2 \theta - Ms(\sin \theta \cos \phi H_x + \sin \theta \sin \phi H_y + \cos \theta H_z), \quad (2)$$

with K_{eff} the effective out-of-plane anisotropy (given by $K_{eff} = \mu_0 H_k M_S / 2$). By combining equations (1) and (2), we obtain:

$$\Delta\theta = \frac{\cos \theta (\Delta H_x \cos \phi + \Delta H_y \sin \phi) - \Delta H_z \sin \theta}{H_k \cos 2\theta + H \cos(\theta - \theta_H)} \quad \text{and} \quad \Delta\phi = \frac{\Delta H_y \cos \phi - \Delta H_x \sin \phi}{H \sin \theta_H}. \quad (3)$$

Now we will show how to extract the magnitudes of these oscillations from the anomalous Hall voltage. For our x - y configuration (Fig.2 a and b in the main text), the anomalous Hall voltage V_{xy} is :

$$V_{xy} = I R_0 + I R_{AHE} \cos(\theta) + I R_{PHE} \sin^2(\theta) \sin(2\phi), \quad (4)$$

with R_{PHE} the planar Hall effect resistance and R_{AHE} the anomalous Hall effect resistance. R_0 is the x - y resistance due to imperfect cross geometry, which is independent of the magnetization. By taking into account the time modulation of the current at frequency f , we replace: $I \rightarrow I_0 \sin(2\pi f t)$, $\Delta H \rightarrow \Delta H \sin(2\pi f t)$, $\theta \rightarrow \theta + \Delta\theta \sin(2\pi f t)$ and $\phi \rightarrow \phi + \Delta\phi \sin(2\pi f t)$. V_{xy} becomes:

$$V_{XY} = V_0 + V_f \sin(2\pi f t) + V_{2f} \cos(4\pi f t), \quad (5)$$

with:

$$V_f = (R_0 + R_{AHE} \cos \theta + R_{PHE} \sin^2(\theta) \sin(2\phi)) I_0 \quad (6)$$

$$\text{and } V_0 = V_{2f} = \frac{1}{2} (R_{AHE} \sin \theta - R_{PHE} \sin(2\theta) \sin(2\phi)) \Delta\theta I_0 - R_{PHE} \sin^2(\theta) \cos(2\phi) \Delta\phi I_0. \quad (7)$$

We note that V_f signal carries the information of magnetization rotation (θ and ϕ) due to the external field. The amplitude of magnetization oscillations due to current-induced torques ($\Delta\theta$ and $\Delta\phi$) appears only in V_{2f} . We measure V_f and V_{2f} simultaneously using a lock-in amplifier with respect to sweeping external magnetic field.

The current-induced field has two orthogonal contributions, the damping-like (H_{DL}) and field-like (H_{FL}), which can be obtained by sweeping the applied field along or transverse to the current direction. To avoid a multidomain state, the external magnetic field H is applied slightly off-plane with an angle $\delta\theta_H \approx 9^\circ$ in our experiments. When the applied field is parallel to the current direction (along $\pm x$ -axis) *i.e.*, $\theta_H = \frac{\pi}{2} + \delta\theta_H$ and $\phi = \phi_H = 0$, by implementing the variations of $\Delta\theta$ and $\Delta\phi$ (eq.3) in (eq.7), V_{2f} becomes:

$$V_{2f}^{DL} = -\frac{1}{2} \sin(\theta) \left(\frac{H_{DL}}{H_k \cos(2\theta) - H \sin(\delta\theta_H - \theta)} + \frac{2H_{FL}\xi \sec(\delta\theta_H) \sin(\theta)}{H} \right) R_{AHE} I_0. \quad (8)$$

In the similar way, when the external field is applied transverse to the current direction (along $\pm y$ -axis) *i.e.*, $\theta_H = \frac{\pi}{2} + \delta\theta_H$, $\phi = \phi_H = \frac{\pi}{2}$, by implementing the variations of $\Delta\theta$ and $\Delta\phi$ (eq.3) in (eq.7), V_{2f} becomes:

$$V_{2f}^{FL} = \frac{1}{2} \cos(\theta) \sin(\theta) \left(\frac{H_{FL}}{H_k \cos(2\theta) - H \sin(\delta\theta_H - \theta)} + \frac{2\xi H_{DL} \sec(\delta\theta_H) \sin(\theta)}{H} \right) R_{AHE} I_0, \quad (9)$$

where $\xi = \frac{R_{PHE}}{R_{AHE}}$. Its magnitude can be determined with additional measurements of $V_f = \left(\frac{R_0}{R_{AHE}} + \cos\theta + \xi \sin^2(\theta) \sin(2\phi) \right) R_{AHE} I_0$ at $\phi = 45^\circ$.

The values of H_k , $\delta\theta_H$ and $\theta(H)$ can be directly extracted from V_f . First, θ can be directly obtained from v_f (the normalised V_f between +1 and -1) as $\theta = \cos^{-1}(v_f)$. Next, the values of H_k and $\delta\theta_H$ can be extracted from $\cos\theta$ as a function of H , by fitting with the Stoner-Wohlfarth model²,

$$\cos\theta = \frac{f}{6} \pm \frac{1}{6} \sqrt{2f^2 - 18e + \frac{54h_z(1+h_{IP}^2)}{f} - \frac{h_z}{2}}, \quad (10)$$

where $h = \frac{H}{H_k}$ is the normalised applied field with in-plane component $h_{IP} = h \sin(\theta_H)$ and out-of-plane component $h_z = h \cos(\theta_H)$, $d = 1 - h^2$, $e = d \cos(\frac{1}{3} \cos^{-1}(54h_{IP}^2 \frac{h_z^2}{d^3} - 1))$, and $f = \pm \sqrt{9h_z^2 + 6d + 6e}$. A simulated θ and V_f with respect to H/H_k is shown in Fig. S2.

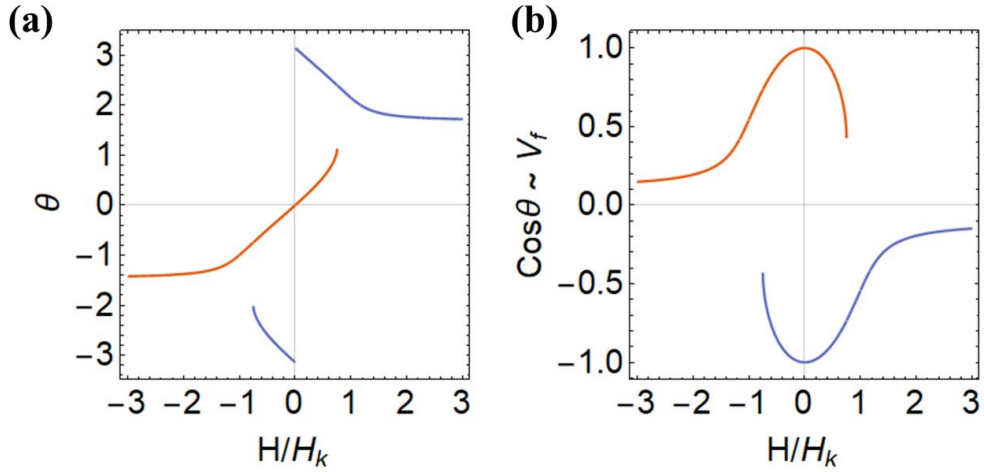


Figure S2. Calculated (a) magnetization tilting away from z- axis (θ) vs H/H_k and (b) First harmonic Hall voltage (V_f) vs H/H_k for fields applied $\theta_H \sim 96^\circ$ angle.

To validate the analytical solution, we simulate V_{2f}^{DL} and V_{2f}^{FL} as a function of the external magnetic field. Here, we set $\delta\theta_H = 11^\circ$, and $\xi=0.1$, comparable to our experiments. V_{2f}^{DL} and V_{2f}^{FL} vs H_x/H_k curves for different H_{FL} and H_{DL} as shown in Figure S3 and S4. Here we note that the peaks in V_{2f}^{DL} change the polarity when the magnetization is reversed (*i.e.* when $H<0$) whereas V_{2f}^{FL} peaks are independent of magnetization direction. The amplitude of V_{2f} peaks predominantly depends on H_{DL} in longitudinal geometry (V_{2f}^{DL}) and on H_{FL} in transverse geometry (V_{2f}^{FL}). A similar behavior in the peak polarities and peak heights is observed in our experiments.

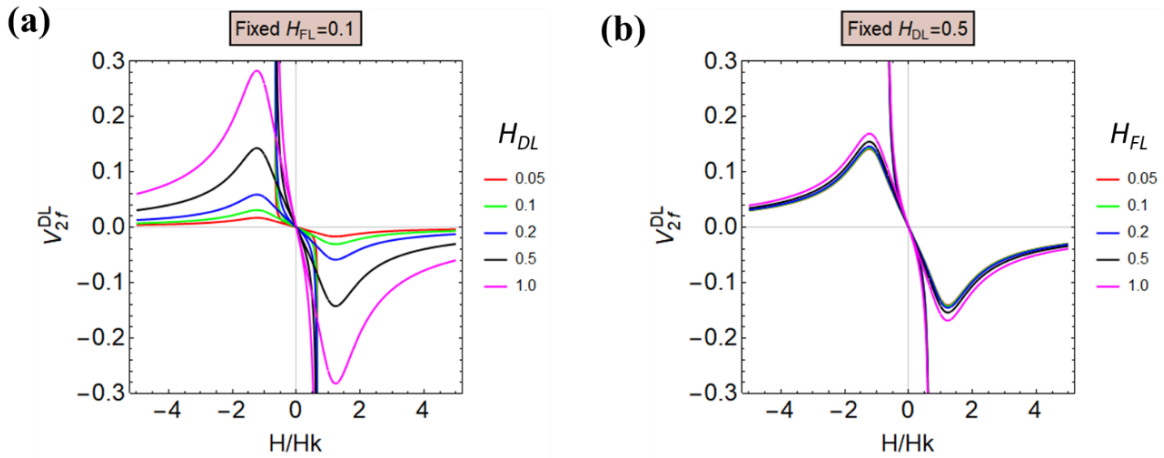


Figure S3. Numerically simulated V_{2f} vs in-plane field in longitudinal geometry using equation (8) for $\delta\theta_H = 11^\circ$, and $\xi=0.1$. (a) V_{2f}^{DL} vs in-plane field for various H_{DL} at a fixed $H_{FL}=0.1$ and (b) for various H_{FL} at a fixed $H_{DL}=0.5$.

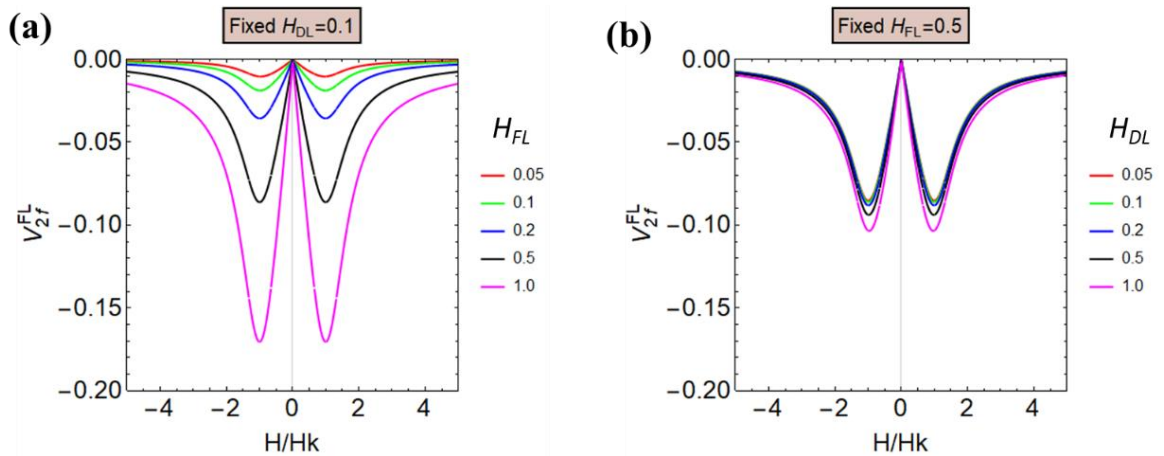


Figure S4. Numerically simulated V_{2f} vs in-plane field in transverse geometry using equation (9) for $\delta\theta_H = 11^\circ$, and $\xi=0.1$. (a) V_{2f}^{FL} vs in-plane field for various H_{FL} at a fixed $H_{DL}=0.1$ and (b) for various H_{DL} at a fixed $H_{FL}=0.5$.

S2. Spin-orbit torques analysis in SiO_x/GdFeCo/Al sample

The 1st (V_f) and 2nd (V_{2f}) harmonic Hall voltages were measured simultaneously with multiple harmonic lock-in amplifier. So far, various regimes of the V_{2f} vs H plots have been used to extract the effective fields^{1,3,4}. Here, we combine all the regimes and perform a full-field fitting method. In other words, we fit the V_{2f} vs H plots from $H=0$ to $H>H_k$. First, we extract θ , $\delta\theta_H$ and H_k from V_f as previously described (eq.10) (Fig.S5(a and c)). Next, by choosing H_{DL} and H_{FL} as free parameters, the experimentally measured V_{2f}^{DL} and V_{2f}^{FL} voltages as a function of the external field are fitted using eq. 8 and eq. 9 (see Fig.S5 b for H_{DL} and Fig.S5 d for H_{FL}). This method allows us to extract H_{DL} and H_{FL} simultaneously from both the geometries. However, the H_{DL} (H_{FL}) extracted from longitudinal (transverse) geometry is more accurate as ξ^*H_{FL} (ξ^*H_{DL}) is much smaller than H_{DL} (H_{FL}) and has trivial effect on the fit if $\xi<<1$. The contribution of ξ is obtained by comparing V_f dependence on in-plane fields applied at azimuthal angle $\phi_H = 0^\circ$ and $\phi_H = 45^\circ$. For the considered sample, ξ is measured to be 0.09. The fittings are performed after subtracting a constant offset from the raw data. We also consider an Oersted field created by the Al cap (assuming 3 nm of the Al cover is oxidised in agreement with the EELS observations). The value of H_k extracted from the $V_f(H)$ fitting are given in the main text Fig 1b.

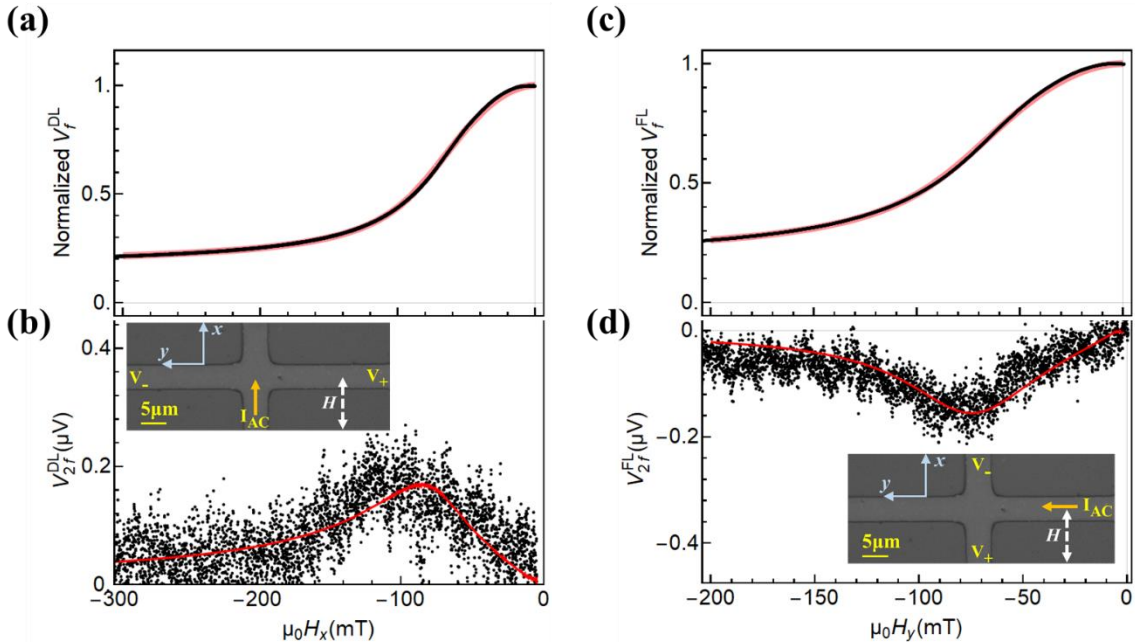


Figure S5. (a) First and (b) second harmonic Hall voltage as a function of external field in longitudinal geometry. (c) First and (d) second harmonic Hall voltage as a function of external field in transverse

geometry. The shown data is measured at $T-T_M = -35\text{K}$ and for a current density $1 \times 10^{10} \text{ A/m}^2$. The red lines are the fits. Insets are the illustration of measurement technique in longitudinal and transverse geometries.

Furthermore, we have compared the results of the fitting by employing the J. Kims' fitting method¹. This method relies on small angle approximation of net magnetization *i.e.*, the magnetization remains close to the easy axis ($\theta \ll I$). With this approximation, the effective fields can be extracted from V_f and V_{2f} data using a relation

$$\Delta H_x \approx \frac{\left(\frac{\partial V_{2f}^{DL}}{\partial H_x} \right)}{\left(\frac{\partial^2 V_f^{DL}}{\partial H_x^2} \right)} \quad \text{and} \quad \Delta H_y \approx \frac{\left(\frac{\partial V_{2f}^{FL}}{\partial H_y} \right)}{\left(\frac{\partial^2 V_f^{FL}}{\partial H_y^2} \right)}, \quad (11)$$

with $H_{DL} = -2 \frac{\Delta H_x + 2\xi \Delta H_y}{1-4\xi^2}$ and $H_{FL} = -2 \frac{\Delta H_y + 2\xi \Delta H_x}{1-4\xi^2}$. An example of various fittings is shown in Figure S6. The blue fitting is Kim's method, assuming a negligible ξ . The red and orange fittings are our analysis methods considering that the longitudinal geometry is sensitive to both H_{DL} & H_{FL} (red) and only to the H_{DL} *i.e.*, $H_{FL}=0$ (orange). The red and orange fittings are quite similar as expected and explained in section S2. All the methods give small but significant effective fields within the error bars as shown in Figure S7. However, the values extracted using Kim's method are noisier.

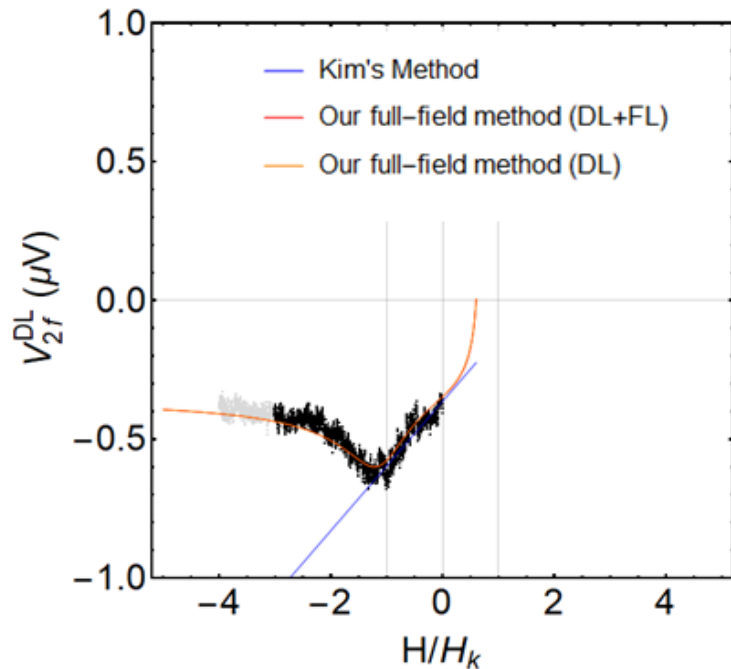


Figure S6. Second harmonic Hall voltage as a function of external field in longitudinal geometry. Our full-field fitting method considering the existence of both H_{DL} & H_{FL} , and considering that the longitudinal geometry is only sensitive to the H_{DL} , *i.e.*, $H_{FL}=0$ are shown by red and orange, respectively. Kim's method is shown in blue.

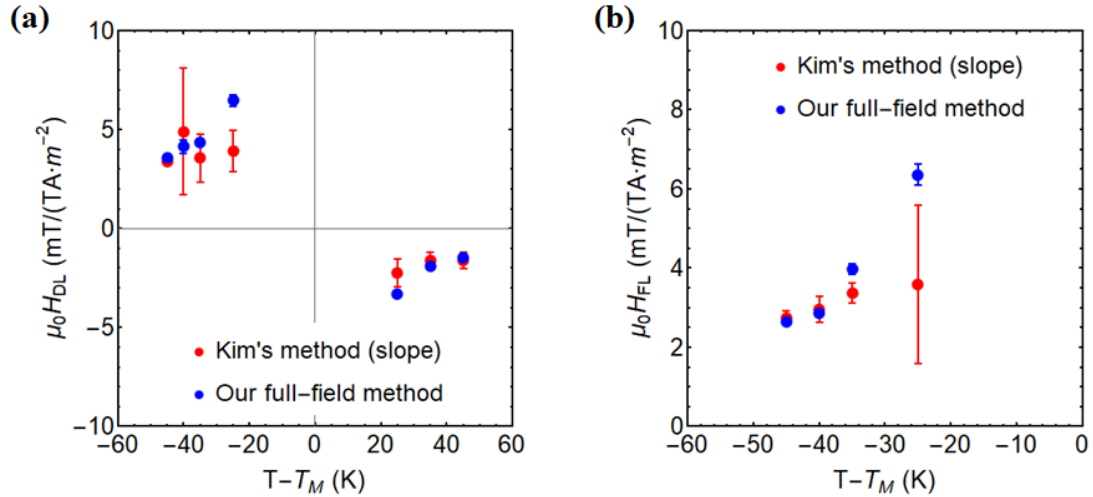


Figure S7. Comparison between two analysis methods. **(a)** H_{DL} and **(b)** H_{FL} effective fields per current density as a function of $T - T_M$, extracted using our method (blue) and Kim's method (red)

As mentioned in the main text, we could not measure H_{FL} in transverse geometry due to noisy data above room temperature. The raw data for all the temperatures is shown in figure S8. During the experiments, we interchanged the current and voltage channels instead of rotating the sample, due to the experimental set-up restrictions. The two channels had very different resistance, 3.9 k Ω in longitudinal geometry and 6.5 k Ω in transverse geometry. The larger resistance of the current channel in transverse geometry might be a possible reason for the increasing noise with temperature. However, the exact reason is unknown.

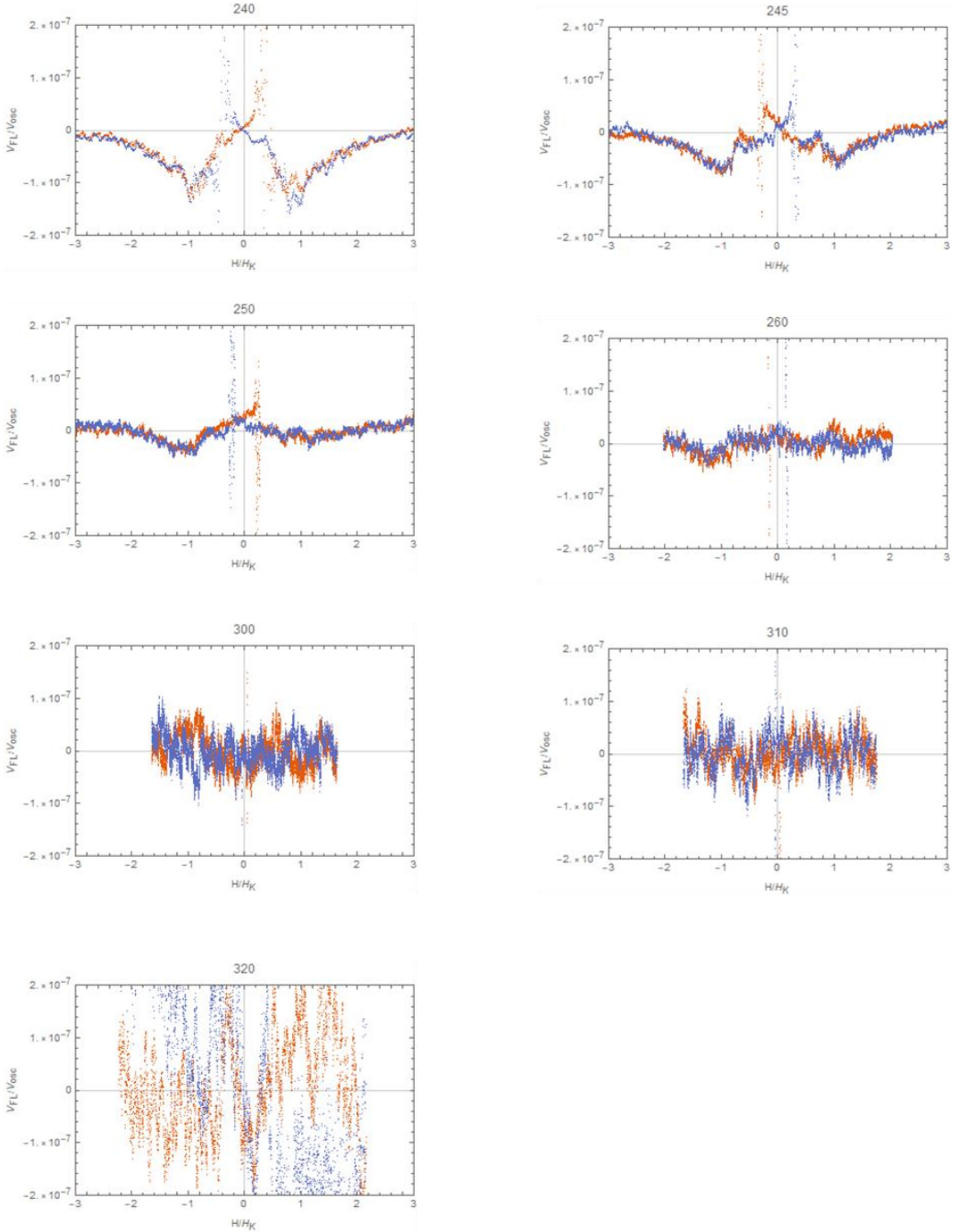


Figure S8. Second harmonic Hall voltage signal at various temperatures in transverse geometry. The noise increases with the temperature.

S3. Spin-Orbit torques analysis in SiO_x/GdFeCo/ Pt sample

For the Pt capped sample, as the signals are quite larger, we use Kim's analysis method¹. Figure S9 (a) shows the behavior of V_f (khaki) and V_{2f} (black) with an external magnetic field in longitudinal geometry. Overlaid red (up magnetization) and blue (down magnetization) lines show the data used for the analysis. The V_f (V_{2f}) shows quadratic (linear)

dependence on in-plane fields. The effective fields are extracted using equation (11). $\xi = 0.08$ is obtained. The effective fields are plotted in Figure S9(b).

The H_{DL} vs temperature behavior is similar to the Al capped sample *i.e.*, the effective fields diverge at T_M , where, $M_s \rightarrow 0$. We estimated the spin Hall angle (θ_{SH}) using the relation $\theta_{SH} = \frac{2e}{\hbar} \frac{\mu_0 H_{DL}}{J} M_s t$ and plotted as a function of temperature in Figure S9(c). The spin Hall angle is found to be independent of temperature with a median value $\theta_{SH} \approx -0.12$. The sign of spin Hall angle is in agreement with SiOx/Co/Pt structures and opposite to that of the SiOx/GdFeCo/Al sample. The magnitude of the θ_{SH} is about 100 times higher than in SiOx/GdFeCo/Al sample.

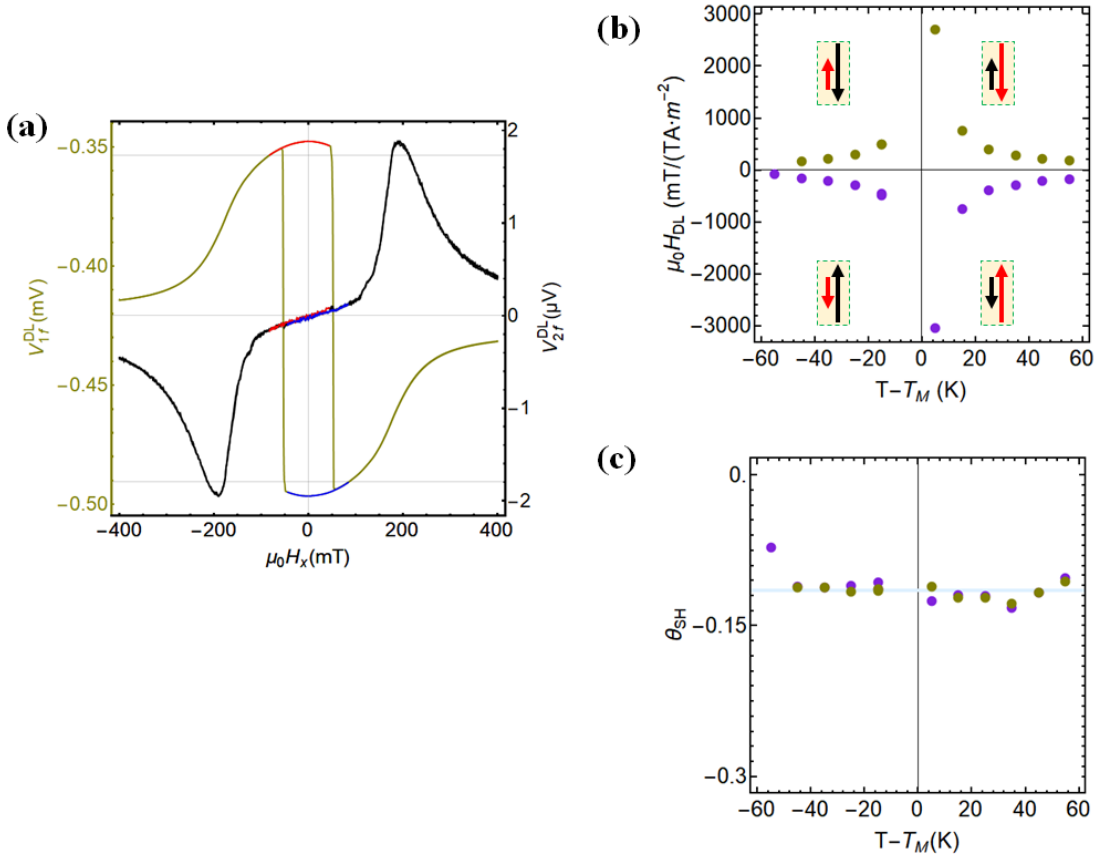


Figure S9. (a) First (khaki) and second (black) harmonic Hall voltage as a function of external field in longitudinal geometry for SiOx/GdFeCO/Pt sample below magnetic compensation temperature. (b) The HD_L for net magnetization up (purple) and down (khaki) as a function of temperature. The inset shows the direction of Gd (black) and FeCo (red) magnetic moments. (c) θ_{SH} vs temperature. The horizontal blue line corresponds to the median value of θ_{SH} .

Figure S10(a) shows V_f (khaki) and V_{2f} (black) as a function of external magnetic field in transverse geometry. The H_{FL} is extracted using equation (11) and plotted as a function of temperature in Figure S10(b). H_{FL}/J also diverges at T_M . Sign of the H_{FL} is independent of

magnetization direction. If we assume that H_{FL} originates from the Rashba effect, the product $\alpha_R P \approx -2.5 \times 10^{-32} Jm$ is negative and, again much bigger than if compared in SiOx/GdFeCo/Al sample ($\approx 7 \times 10^{-33} Jm$).

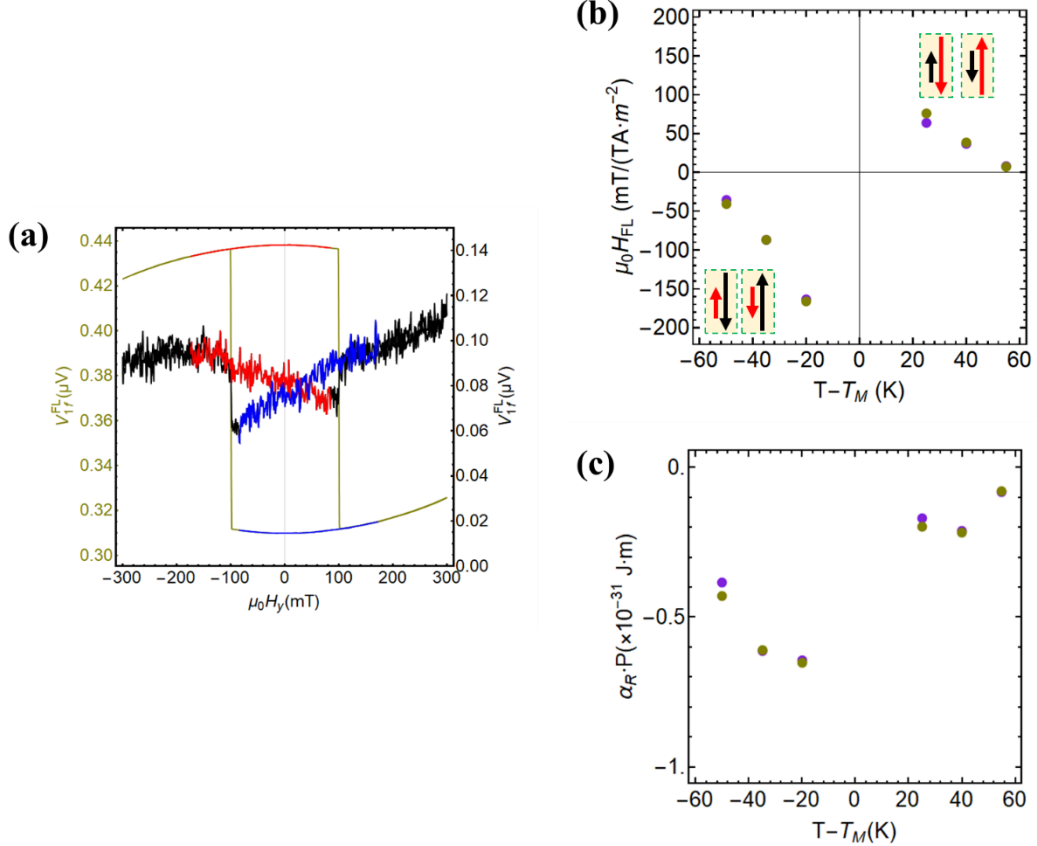


Figure S10. (a) First (khaki) and second (black) harmonic Hall voltage as a function of external field in transverse geometry for SiOx/GdFeCo/Pt sample below compensation ($T - T_M = -35\text{K}$). (b) The H_{FL} for net magnetization up (purple) and down (khaki) as a function of temperature. The inset shows the direction of Gd (black) and FeCo (red) magnetic moments. (c) $\alpha_R P$ vs temperature.

S4. XMCD-PEEM imaging on SiOx/GdFeCo/Al sample.

We used X-ray magnetic circular dichroism (XMCD) experiments combined with PEEM at the BL24-CIRCE beamline of the ALBA synchrotron (Barcelona, Spain) to investigate the DWs internal structure in single layer ferrimagnets. The technique uses helicity dependent absorption of circularly polarized X-rays by magnetic moments those are parallel to the beam wave vector (\vec{k}_b). Therefore, the image contrast (I_{XMCD}) is proportional to the projection of magnetization along the beam direction: $I_{XMCD}(x) = \vec{m} \cdot \vec{k}_b$. The magnetization profile of a DW can be written in polar coordinates as: $m = (\sin(\theta) \cos(\phi), \sin(\theta) \sin(\phi), \cos(\theta))$ with $\theta = 2 \arctan \left[\exp \left(\pm \frac{x}{\Delta} \right) \right]$ and $k_{X-Ray} = (\sin(\theta_b) \cos(\phi_b), \sin(\theta_b) \sin(\phi_b), \cos(\theta_b))$, which gives:

$$I_{XMCD}(x) = \cos(\phi - \phi_b) \sin \theta_b \operatorname{sech}\left(\frac{x}{\Delta}\right) - \cos \theta_b \tanh\left(\frac{x}{\Delta}\right). \quad (12)$$

Figure S11 shows XMCD profiles of an up-down domain wall with right-handed Néel ($\phi = 0$), Bloch ($\phi = \pm \frac{\pi}{2}$) and left-handed Néel ($\phi = \pi$) DWs when $\theta_b = 16^\circ$. The XMCD contrast due to in-plane magnetisation is about ~ 3.6 times higher than out-of-plane magnetisation for $\phi - \phi_b = 0$ or π . Therefore, the method allows us to probe in-plane & out-of-plane components with high lateral spatial resolution down to 25nm^5 .

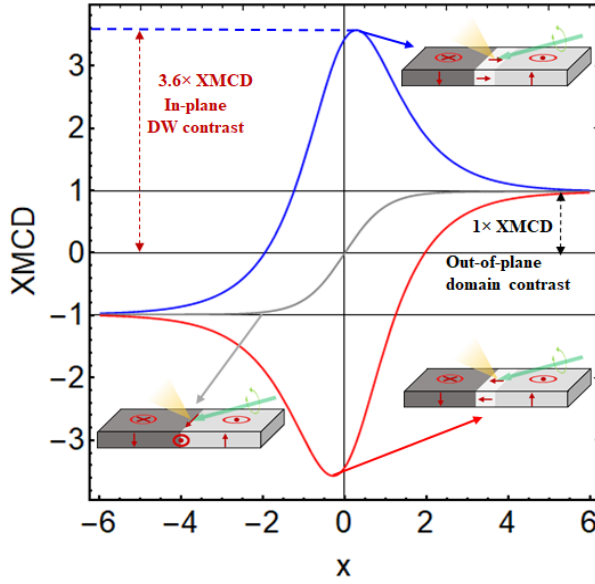


Figure S11. Calculated XMCD-PEEM intensity of an Up-Down domain with right-handed Neel ($\phi = 0$), Bloch ($\phi = \pm \frac{\pi}{2}$) and left-handed Neel ($\phi = \pi$) DWs. The DWs magnetization profiles are shown in insets.

Figure S12 shows X-ray absorption spectra (XAS) as a function of photon energy for left handed and right-handed circularly polarized X-rays. The XMCD signal, *i.e.* ratio of difference between right and left handed circularly polarized beams to their sum, shows a maxima at photon energy 1178.7 eV which is characteristic of $M_{4,5}$ edge of Gd. In the article, the XMCD-PEEM images are acquired at 1178.7 eV. Note that the chirality of DWs can be determined independently of the XMCD sign.

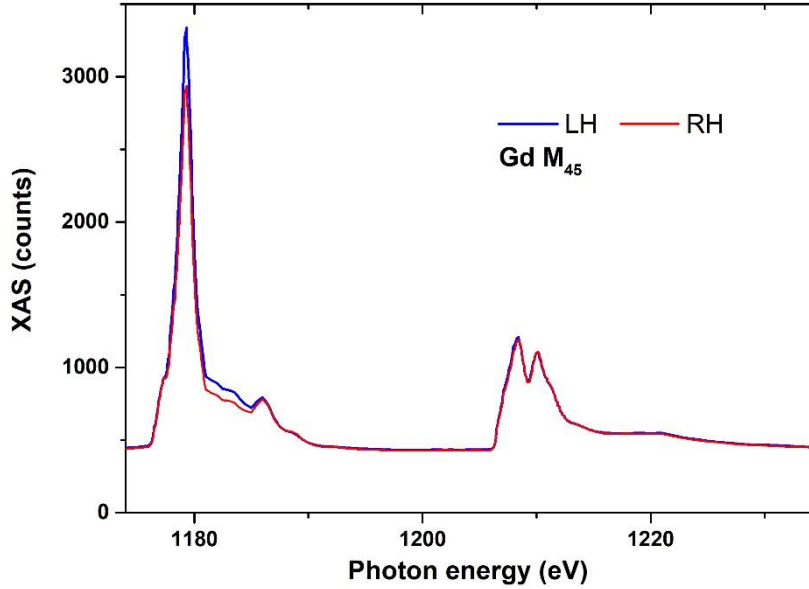


Figure S12. X-ray absorption spectroscopy (XAS) for Gd at room temperature. The red and blue curves show the absorption of right-handed (RH) and left-handed (LH) circularly polarized X-rays.

The microscope has a finite resolution r . Therefore, we account for the microscope resolution (r) by convolving the expected XMCD profile of the DW with a Gaussian function:

$$(I_{XMCD} \star G_r)(x) \triangleq \cos(\phi - \phi_b) \sin(\theta_b) \int_{-\infty}^{\infty} \operatorname{sech}\left(\frac{\eta}{\Delta}\right) G_r(x - \eta) d\eta - \cos(\theta_b) \int_{-\infty}^{\infty} \tanh\left(\frac{\eta}{\Delta}\right) G_r(x - \eta) d\eta. \quad (13)$$

The Néel nature of the DW can be seen directly in the intense bright and dark contrast of the DWs perpendicular to the X-rays. The DWs internal structure can be further analysed by fitting the line-scans with equation (13) as shown in Figure 3 of the main text. Few additional DWs profiles are shown in Figure S13. A dip or a peak indicates that the DWs magnetization lies along the X-ray (yellow regions), the Néel DW structure. When the X-ray is parallel to the DW length, peak or dip is not observed, again in the agreement with Néel DW profile (no peak and dip is expected when the DW magnetization is perpendicular to the X-ray direction).

The line-scan is also performed at the edge of a gold pad on the same image into Figure 3 of main text as shown in Figure S13(d). The XMCD contrast does not show any peak or dip at the edge of the gold pad, verifying that the observation of peak and dip is not an artifact.

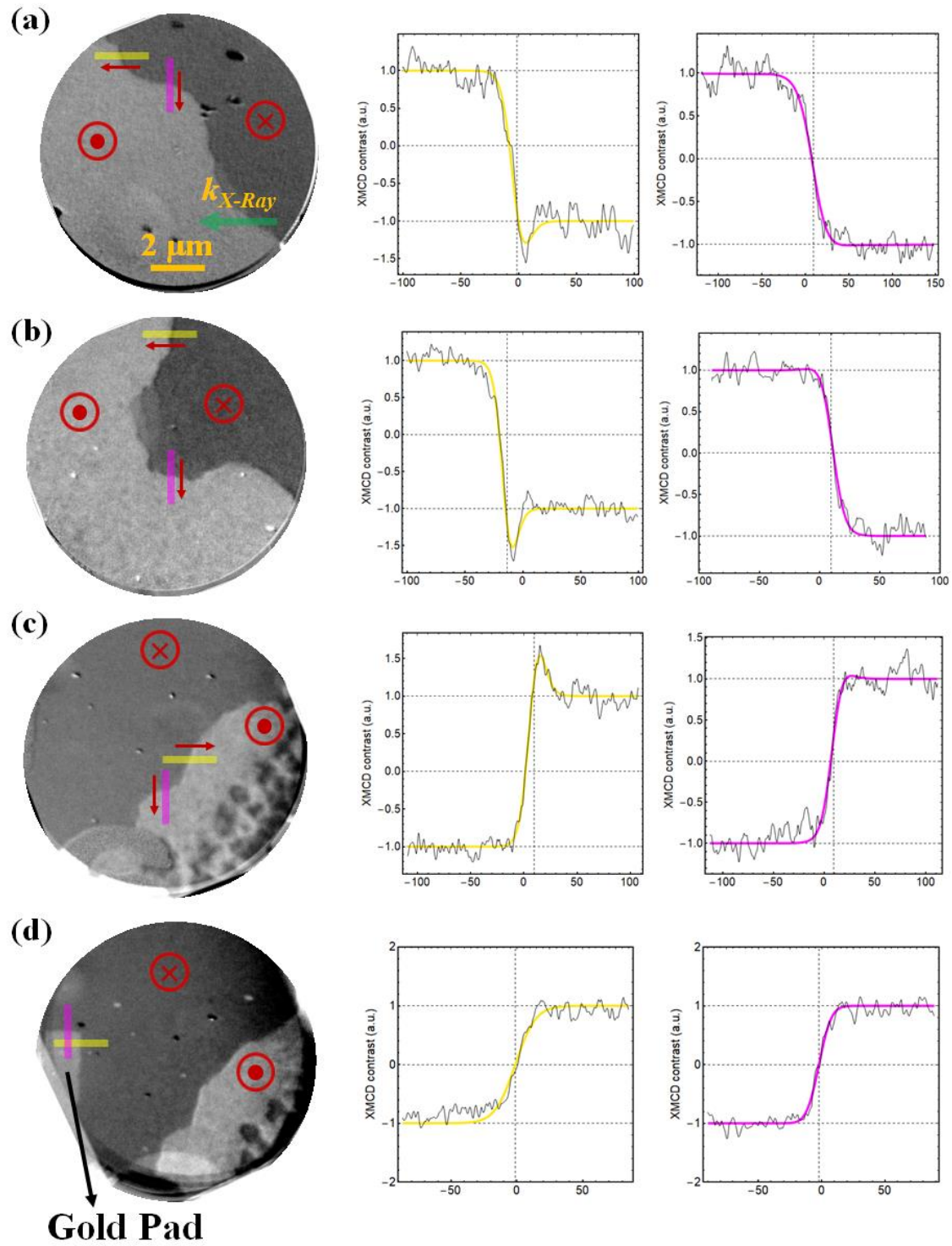


Figure S13 Multi domain XMCD-PEEM images at different parts of the sample at T=230 K. XMCD intensity profiles (black lines) averaged over the yellow and magenta regions are shown next to each XMCD-PEEM image. The green arrow indicates the incident X-Ray direction. The magnetization direction in domains and domain walls are shown by red.

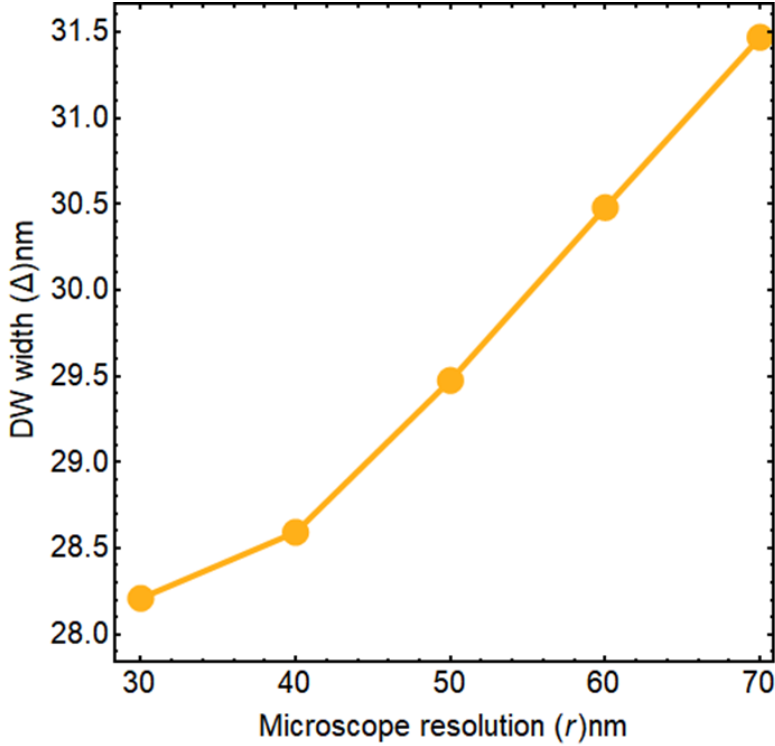


Figure S14. The DW width (Δ) as a function of microscope resolution (r).

In the analysis of Néel DWs XMCD intensity profile, the microscope resolution (r) is measured on dust particles on the image. Figure S14 shows the sensitivity of the extracted DW width assuming the r is a fixed parameter with values between 30 to 70 nm. The results show that microscope resolution has a very weak impact on the DW width parameter, $\Delta \approx 29 \pm 1$ nm.

S5. Spin wave spectroscopy to quantify DMI in SiOx/GdFeCo/Al samples

Brillouin light scattering (BLS) technique in Damon-Eshbach (DB) geometry is used to quantify the DMI in our samples. An in-plane magnetic field (H_{ex}) is applied to saturate the magnetization along the -y-axis, and thermally activated spin waves propagating along x -direction are probed using a green laser of $\lambda = 532$ nm. The spectra for different wave-vectors ($k_{sw} = 4\pi \sin\theta/\lambda$ correspond to $\theta = 10^\circ, 20^\circ, 30^\circ, 45^\circ$ and 60°) are recorded at $T=293$ K in 180° backscattered geometry and fitted with Lorentzian asymmetric function (an example is shown in Figure 4(a) of main text): $I(f) = \frac{A+c(f-f_0)}{(f-f_0)^2+B^2}$. In addition, when the sample signal was very low, a background (e.g. from the detector's dark current) was included in the fit.

The total momentum is conserved in backscattering events of the light which results in Stokes and anti-Stokes peaks in the spectrum. The position of Stokes and anti-Stokes peaks

depends on the energies of the forward and backward propagating SWs. If they have the same energy, the Stokes and anti-Stokes peaks should be symmetric in frequency. However, we observed an asymmetry in the resonant frequencies, which arises due to DMI: $f_S = f_0 \pm f_{DMI}$ and $f_{AS} = f_0 \mp f_{DMI}$. The positions of Stokes and anti-Stokes peaks are extracted by fitting the spectra as shown in Fig.4 of the main text.

The spin wave dispersion relation is given by^{6,7}:

$$f_0 = \frac{|f_S| + |f_{AS}|}{2} = \frac{\gamma \mu_0}{2\pi} \sqrt{(H_{ex} + Jk_{sw}^2 + P(k_{sw}t)M_s)(H_{ex} - H_{keff} + Jk_{sw}^2 - P(k_{sw}t)M_s)}, \quad (14)$$

Where, f_0 is the resonant frequency in the absence of DMI, $M_s = |M^{FeCo} - M^{Gd}|$ is the net magnetization, $J = \frac{2A}{\mu_0 M_s}$, A is the exchange stiffness constant, H_{keff} is the effective anisotropy field, $P(k_{sw}t) = 1 - \frac{1 - \exp[-k_{sw}t]}{k_{sw}t}$, γ is the effective gyromagnetic ratio of the alloy. f_0 as a function of k_{sw} is plotted in Figure S15. The extrapolation of these curves to $k_{sw} \rightarrow 0$ only depends on γ and H_{keff} as:

$$f_{0(k_{sw} \rightarrow 0)} = f_{FMR} = \frac{\gamma \mu_0}{2\pi} \sqrt{H_{ex}(H_{ex} - H_{keff})}, \quad (15)$$

The fit (fig. S15) gives $\frac{\gamma}{2\pi} = 9.95 \pm 0.15 \frac{GHz}{T}$, yielding a g -factor ≈ 0.71 and $\mu_0 H_k = 0.18$ T at T=293 K. Anisotropy field was extracted from a linear fit to FMR frequency *vs* applied field plot and found to be in agreement with that extracted from AHE measurements on devices. The fit for the full range of k_{sw} gives the $A = 0.83$ pJ/m.

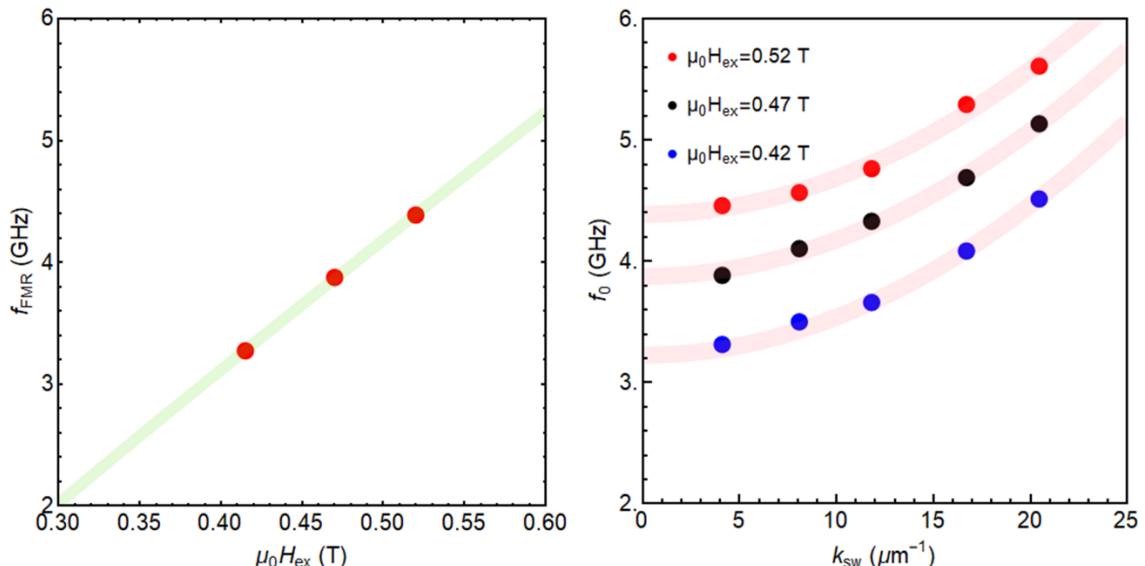


Figure S15. Left: Ferromagnetic resonance frequency *vs* applied external magnetic field extracted from the right panel. The line is the fit to the Kittel Eq.15 to extract H_k . **Right:** The averaged resonant

frequency (f_0) vs k_{sw} for three different in-plane magnetic fields: $\mu_0 H_{ex} = 0.42$ T (blue), 0.47 T (black), and 0.52 T (red). The lines are the fits to Eq.14 to obtain γ , and A .

A relation directly relates the asymmetry in the frequency with DMI constant^{8,9}:

$$f_{DMI} = \frac{|f_S| - |f_{AS}|}{2} = \frac{\gamma}{\pi M_s} D k_{sw}. \quad (16)$$

By using the values of γ and M_s , the slope of Δf vs k_{sw} plot gives the value of DMI constant (Fig.4(b and c) of main text). As the ferrimagnets are very sensitive to the heating effects, the laser power was reduced until no effect of the laser power was detected (0.1 mW).

S6 STEM and EELS studies on SiO_x/GdFeCo/Al sample

Cross-sectional electron-transparent samples were prepared for electron spectro-microscopy (STEM-EELS) studies by focused ion-beam on a SIOS dual-beam platform (FEI-Thermofischer). The local elemental analysis of the SiO_x/GdFeCo/AlO_x nanostructure was performed on a C3/C5-corrected Nion UltraSTEM 200 operated at 100 kV with 30mrad convergence angle, 50mrad EELS collection angle, and around 50-70 pA of probe current. The microscope was equipped with a Medipix3 direct electron detection (Merlin EM Quantum Detectors). EELS spectra were gain-corrected with a gain reference acquired prior to the experiments. Spectrum-images were denoised using a combination of Principal Component Analysis (PCA) (remaining the first 20 components) and denoising of the components maps by BM3D (the state-of-the-art image denoising algorithm¹⁰, followed by an inverse PCA to reconstruct a filtered spectrum-image. The background was fitted with a power law on an energy window located before the edge and subtracted from the EELS spectra. The absorption edges were integrated over 25 eV for Fe-L_{2,3} and Co-L_{2,3} edges, over 40 eV for Al K and over 60 eV for Gd M_{4,5} edges.

The low-magnification HAADF image in Fig. S16 depicts an homogeneous GdFeCo layer over several hundreds of nm along the entire film without any apparent defects. The HAADF contrast originates mainly from $\sim Z^2$, *i.e.* heavy atoms (e.g. RE) arise brighter contrasts and lighter atoms (e.g. Al) give darker contrasts.

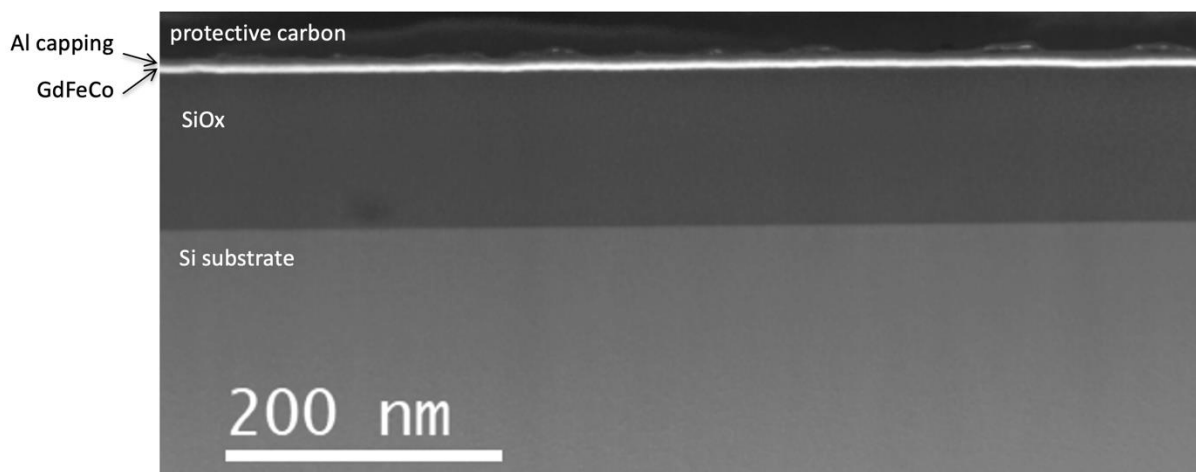


Figure S16 Low-magnification HAADF image of the Si/SiOx/GdFeCo/Al sample

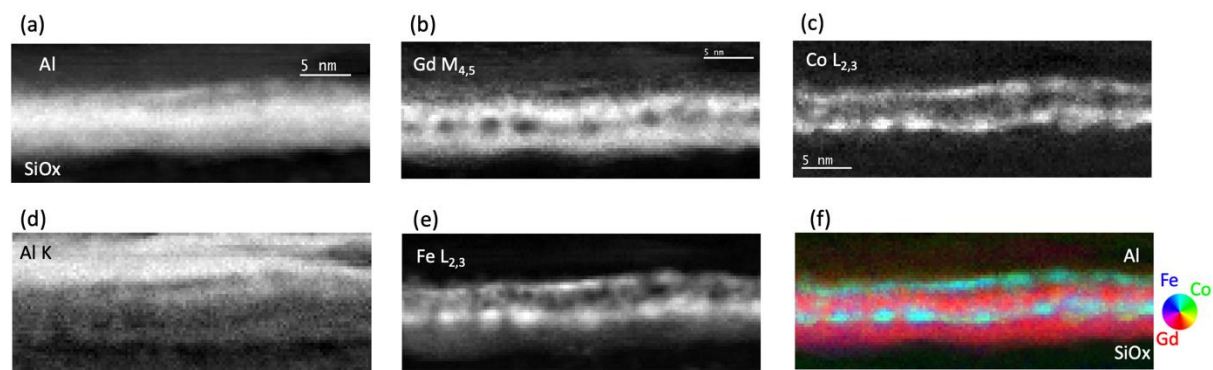


Figure S17 Elemental maps of the SiOx/GdFeCo/Al sample: (a) HAADF intensity map acquired simultaneously with the EELS spectrum-image. (b) Gd M_{4,5}, (c) Co L_{2,3}, (d) Al K, (e) Fe L_{2,3} and (f) superimposed “false color” Gd (red) Fe (blue) and Co (green) maps.

S7 References

1. Kim, J. *et al.* Layer thickness dependence of the current-induced effective field vector in Ta|CoFeB|MgO. *Nat. Mater.* **12**, 240–245 (2013).
2. Wood, R. Exact solution for a Stoner-Wohlfarth particle in an applied field and a new approximation for the energy barrier. *IEEE Trans. Magn.* **45**, 100–103 (2009).
3. Wu, H. *et al.* Spin-Orbit Torque Switching of a Nearly Compensated Ferrimagnet by Topological Surface States. *Adv. Mater.* **31**, 1–6 (2019).
4. Garello, K. *et al.* Symmetry and magnitude of spin-orbit torques in ferromagnetic heterostructures. *Nat. Nanotechnol.* **8**, 587–593 (2013).
5. Aballe, L., Foerster, M., Pellegrin, E., Nicolas, J. & Ferrer, S. The ALBA spectroscopic

LEEM-PEEM experimental station: Layout and performance. *J. Synchrotron Radiat.* **22**, 745–752 (2015).

6. Moon, J. H. *et al.* Spin-wave propagation in the presence of interfacial Dzyaloshinskii-Moriya interaction. *Phys. Rev. B - Condens. Matter Mater. Phys.* **88**, 1–6 (2013).
7. Raasch, D., Reck, J., Mathieu, C. & Hillebrands, B. Exchange stiffness constant and wall energy density of amorphous GdTb-FeCo thin films. *J. Appl. Phys.* **76**, 1145–1149 (1994).
8. Belmeguenai, M. *et al.* Interfacial Dzyaloshinskii-Moriya interaction in perpendicularly magnetized Pt/Co/AlOx ultrathin films measured by Brillouin light spectroscopy. *Phys. Rev. B - Condens. Matter Mater. Phys.* **91**, 1–4 (2015).
9. Di, K. *et al.* Direct observation of the Dzyaloshinskii-Moriya interaction in a Pt/Co/Ni film. *Phys. Rev. Lett.* **114**, 1–5 (2015).
10. Davob, K., Foi, A., Katkovnik, V. & Egiazarian, K. The Development And Characterization Of Next Generation Endovascular Devices Using Thin Film Nitinol Notes The Development And Characterization Of Next Generation Endovascular Devices Using Thin Film Nitinol Notes. *IEEE Trans. Image Process.* **16**, 1–2 (2007).